# NOx formation of spray combustion at different OH models under equilibrium oxygen conditions

*Sarah Falih Kareem [1]\* , Ahmed Abed Al Kadhem Majhool [1]* iD *, and Faris Alqurashi [2]*

[1]*Mechanical Engineering Department, College of Engineering, University of Al-Qadisiyah, Iraq.*
[2]*Mechanical Engineering Department, University of Bisha, 67714, Bisha, Kingdom of Saudi Arabia.*

## ARTICLE INFO

## ABSTRACT

This work employs partial and non-OH models to mimic 2D steady-state spray combustion. The study examines the status of the partial OH model following the NOx forecast, comparing it to the non-model. It assumes that the O model is in equilibrium with the predicted NOx. The study assesses the numerical models by using data from Mao et al. (35). This study used n-pentane as the fuel and ambient air as the oxidant in a turbulent flame characterized by non-premixed combustion. The mixture fraction-probability density function model is used to solve chemical kinetics. Fluent 15.0 software performs numerical simulation of two-phase flow and combustion modeling for pollutant formation. The k−ε turbulence model was used to solve the conservation equations for mass, momentum, and energy in turbulent flow fields. A simulation was performed using a thermal NOx mechanism to compute NOx formation. This study investigated the velocity components in the gas phase, the mass fraction of NOx, the NOx rate, the turbulence kinetic energy, and the dissipation rate. Due to state stability, the instantaneous and partial OH models were equivalent, whereas the non-OH model was lower than the partial model. The NOx prediction predicted this temperature variation in response to NOx formation. The NOx mass fraction varies by 0.09% between the partial and non-OH models, and the NOx rates exhibit a 0.09% variation between these models. Across all tested domains, the non-OH model effectively decreased all variables, including NOx emissions.

## 1. Introduction

Fossil fuel combustion provides about 90 percent of the world's energy consumption today. The world's increasing need for energy, the limited and rapid reduction of fossil fuel resources, and the environmental problems of these fuels have caused the design of combustion devices with high efficiency on the one hand and low pollutant production on the other. Many researchers and designers of combustion systems are involved [1]. The combustion of fossil fuels leads to the production of considerable pollutants and, finally, the warming of the earth due to the formation of elements such as NOx, CO, and CO2 [2]. During the combustion process, the combination of nitrogen and oxygen in the air forms NO, which quickly transforms into NO2 once it enters the air. Thermal is one of the most important mechanisms among the main pathways for NOx formation. Zeldovich [3]

was the first to propose this mechanism. High temperature and oxygen concentration are important factors in this mechanism; they are involved in most combustion processes. These reactions are also called thermal NO-formation reactions. The formation of nitrogen oxides through the nitrogen molecule necessitates the breaking of strong bonds between nitrogen atoms, resulting in this mechanism's strong dependence on combustion [4]. Therefore, if a method reduces the flame temperature, it is an effective factor in reducing NOx formation. Flameless combustion is one of the important technologies in the field of combustion, which has taken an effective step to increase combustion efficiency and reduce pollutants. The name flameless comes from the flame resulting from flameless combustion Compared to a normal flame, this one exhibits a clear characteristic.

---

---

**Nomenclature**

| | | | | |
|---|---|---|---|---|
| $Cp$ | specific heat (J kg$^{-1}$ K$^{-1}$) | | *Greek symbols* | |
| $C_t$ | Turbulent kinetic energy generation | | μt | The turbulent viscosity |
| $C_P$ | Droplet heat capacity ( $J/kg/k$) | | μ | Molecular viscosity (($kg/m^2s^2$)) |
| $f$ | Mixture fraction | | Φυ | Rayleigh dissipation function in $(kg/(S^2 m))$ |
| $F_i$ | Momentum force (kg m$^{-2}$ s) | | $Gb$ | The effect of buoyancy |
| $h_i$ | Enthalpy of species i | | $CD$ | Drag correlation |
| $hfg$ | Latent heat evaporation ( $J/kg$) | | Re | Reynolds number |
| $g_i$ | Gravitational acceleration ($m/s^2$) | | $U_p$ | Droplet velocity($m/s$) |
| $d$ | Diameter (m) | | $U_i$ | Velocity of air ($m/s$) |
| $K$ | Turbulent kinetic energy | | $\in$ | Turbulence dissipation rate |
| $k$ | Thermal conductivity (W m$^{-1}$ k$^{-1}$) | | $Y_i$ | Mixture fraction of species i |
| $k_r$ | Reversed reaction rate($m^3/gmol-s$) | | $CD$ | Drag correlation |
| $k_f$ | Forward reactions rete ($m3/gmol - s$) | | $D_{im}$ | Diffusion coefficient of mixture |
| $T$ | Temperature (K) | | | |
| $r_t$ | Turbulent Prandtl number | | | |
| $Pr$ | Prandtl number | | *Subscr* | |
| $S_h$ | Volumetric heat source (kg  m$^{-2}$ S) | | CFD | Computational Fluid Dynamics |
| $S_f$ | Momentum source term (kg  m$^{-2}$ S$^{-2}$) | | DOM | Discrete Ordinate Method |
| $S_m$ | Mass to gas-phase (kg m$^{-3}$) | | 2-D | Two dimension |
| $S_{Gλ}$ | Defined source term | | PDF | Probability Density Function |
| $P$ | Static pressure ($kg\ m^{-1}\ s^{-2}$) | | WSGGM | Weighted-sum of gray gases model |

---

Only under special conditions can one see a flame. This type of combustion is also known by other names, such as colorless combustion, slow combustion, and combustion with high-temperature air [5 and 6]. An ideal flameless combustion scheme creates a homogeneous and uniform reaction zone throughout the chamber, effectively diluting the reactants (oxidizer and fuel) and reducing the rate of chemical reactions compared to normal combustions [7]. Flameless combustion is characterized by a uniform temperature distribution with a minimum gradient, and its lower peak temperature compared to normal flames significantly reduces pollutant production [8]. One of the most important parameters in creating flameless combustion is the internal recirculation rate of the combustion products inside the chamber. This is very effective in distributing the reaction zone and reducing the combustion peak temperature. It reaches a temperature higher than the auto-ignition temperature, but it dilutes the reactant mixture before entering the reaction zone [6]. Radiant heat transfer is very important in reactive flows because of the high temperature of the gases resulting from combustion. Therefore, it is crucial to carefully select the appropriate model for radiation modelling in the numerical simulation of combustion problems. Dehghan et al. [9] investigated the effects of radiation parameters on the Nusselt number and dimensionless temperature profile, and they found that thermal radiation will increase the rate of heat transfer. CO2 and H2O are two very important reaction components that make a significant contribution to radiant heat transfer due to high absorption and emission coefficients. The type of radiation model used, as well as how to calculate absorption and emission coefficients, are the most important factors in accurately predicting radiation heat transfer. Shakeel et al. [10] used different radiation models with different mechanisms to determine the most effective radiation model for numerical modelling. They investigated methane-oxygen combustion in a gas turbine's combustion chamber. Bardbar's [11] proposed WSGGM model yielded the best results in predicting the temperature of the combustion chamber. Silva [12] also investigated the effects of radiation on methane combustion using the WSGGM model. His findings revealed that radiation is critical for the

chamber's temperature, but less so for the concentration of reaction components. The role of the geometrical parameters of the chamber in the characteristics of flow and combustion in the flameless combustion regime is very important. Sabbagh and Rahbar [13], who examined three geometric shapes for the flare opening, including cylindrical, open cone, and closed cone shapes, concluded that the cone geometry with the open air nozzle opening provides more favorable conditions for combustion. Yaoji et al. [14] investigated the effect of chamber shape on flameless combustion characteristics by changing the angle between the lateral and transverse walls of the chamber. To achieve flameless combustion, increase this angle and change the shape of the chamber to a divergent state, resulting in stronger recirculation of combustion products, a lower temperature gradient, and a wider reaction zone. In a scramjet engine combustion chamber, Zahidzadeh and Amy [15] compared cross- and parallel sprays. According to their findings, the proper mixing of fuel and air has a significant impact on efficient combustion. In cross-injection, the depth of fuel penetration is greater, and the combination is more suitable than in parallel injection mode. Jamie et al. [16] discovered that changing parameters such as the external diameter and the angle of the air and fuel injection nozzles have a significant effect on the penetration distance of the fuel flow, as well as the product recirculation rate (two important features in flameless combustion). Pengfi et al. [17] looked at the effective parameters of the Reynolds number, like fuel and air inlet nozzles. They found that flameless combustion only happens in the studied combustion chamber when the Reynolds number goes over a certain value. Jiyanchun et al. [18] also changed the geometric features of the inlet nozzles to study how the speed of the fuel and air jets affected flameless combustion. They found that in situations where the momentum rate is higher than a critical value, the combustion regime changes from normal flame to flameless combustion. In a numerical study, Liubo et al. [19] investigated the effect of the diameter and number of air nozzles on the combustion chamber's performance. The study's findings showed that reducing the nozzle diameter increased the momentum of the air jet, and increasing the number

of air spraying nozzles increased combustion efficiency. Perone et al. [20] used a new concept of configuring an industrial furnace, including five chambers and three exits for combustion products, and provided access to flameless combustion using pure oxygen. The reduction of NOx emissions was also one of his other results was a reduction in NOx emissions. Considering the recent research and the importance of the industry's role in producing pollutants and harming the environment, investigating the geometric parameters involved in the performance of industrial combustion chambers needs more and more complete study. B.M. Masum et al. [21] They conducted an examination of various fuel composition engine parameters and analyzed the impact of engine modifications on the generation of NOx. Additionally, we explored a mathematical method for predicting NOx levels using ethanol. Hydrous ethanol, as opposed to anhydrous ethanol, has the potential to provide improved outcomes in these engines, namely a reduction in NOx emissions and enhanced engine performance. Ethanol has a slightly lower heating value, which is an issue. Damijan Cerinskia et al. [22] Analyzed quantitatively Increasing the number of nozzle holes and ensuring their accurate placement may lead to a 60% reduction in emissions. They might attribute the aforementioned behavior to the specific formation of spray clouds and smaller areas with high temperatures. Saurabh Sharma et al. [23] found that, in flameless combustion mode, coarser sprays significantly increased the acoustic emissions, caused a somewhat non-uniform temperature distribution, and increased the CO and NOx emissions. Myles D. Bohon et al. [24] conducted an investigation into the emission of extremely low levels of nitrogen oxides (NOx) resulting from the burning of fuel with a high oxygen mass fraction. They specifically selected glycerol as the fuel and compared the results with those obtained from diesel combustion under identical conditions, namely a high swirl turbulent spray flame. The results of this study indicate that glycerol combustion results in NOx emissions that are up to one order of magnitude lower than those seen in diesel fuel. Mingchen Xu et al. [25] This study, using numerical methods, investigates the viability of using fuel-rich/lean technology to further reduce NOx emissions from a semi-industrial-sized coal MILD (moderate and intensive low oxygen dilution) combustion furnace**.** The results show that both the IFR and OFR designs effectively lower NOx emissions even more than the reference example, which includes both the fuel and thermal pathways. In general, this study compares NOx emissions under equilibrium oxygen conditions between two OH models (partial and none), as well as situations that occur before and after NOx prediction. The study shows that the partial and instantaneous OH models are the same if everything stays the same. The none-OH model will produce less NOx than the partial model, as shown by a numerical calculation of NOx production for C5H12 using the thermal NOx process. In this case, the OH model has a minimal impact on NOx generation. Along with the NOx prediction, the temperature also changes, although it remains constant with the OH model variance. Upon examining the emissions for each factor in this article, it became evident that no OH model could be the optimal choice.

## 2. Mathematical model

The numerical model is based on a conventional formulation of the Eularian gas phase and the Lagrangian liquid phase. The Lagrangian technique establishes the connection between the two phases through interaction term sources derived from the liquid phase data.

### 2.1 Liquid phase

The liquid-phase droplets determine the start of solutions by combining the force balance with the Lagrangian method. The primarily spherical, suitably diluted, and smaller liquid droplets in the area of interest support this approach. It explains the package of ordinary differential equations for mass, momentum, and heat transfer. The balancing force of the droplet particles is identified [26] [27]

$$\frac{du_p}{dt} = f_D(u - u_p) + \frac{g_{x(\rho_p-\rho)}}{\rho_p} + \frac{\rho}{\rho_p} u_p \frac{\partial u}{\partial x_i} \tag{1}$$

$$f_D = \frac{18\mu}{\rho_p d_p^2} \frac{c_D R_e}{24} \tag{2}$$

$$R_e = \frac{d_p \rho |u_p - u|}{\mu} \tag{3}$$

The gravitational force acting on the droplets are $(g_x \,(\rho\_\,p_g)\,/\rho\_\,p$, where the droplets velocity equals $u_p$ in (m/s$^2$), and the drag force action per unit mass of the particle is $f_D \,(u - u_p)$ in (m /s$^2$). An additional force on the other side is the third term. produced by the fluid's disparity in pressure. $\frac{du_p}{dt}$ Term indicates the particle's rate of evaporation. gravity is $g_x$ in (m /s$^2$), droplet diameter is $dp$, and drag coefficient is $CD$. The heat equilibrium is used to calculate the amount of heat moved from the liquid to the gaseous phase. One of the most essential considerations is to look at the effect of the drag force of the particles. To determine the drag force coefficient character, drag correlation [27]

$$CD = a_1 + \frac{a_2}{R_e} + \frac{a_3}{R_e^2} \tag{4}$$

$(a_1, a_2, a_3)$ The rate of vaporization is determined by the variation in vapour concentrations between the surface of a droplet and the gas phase. The volumetric source's term, shown as $S_h$, can be calculated

$$s_h = \left[ \frac{\bar{m}_p}{m_{p.o}} cp\Delta T_P + \frac{\Delta m_p}{m_{p.o}}(-h_{fg} + \int_{T_{ref}}^{T_p} C_{p.i}\, dt) \right] \tag{5}$$

### 2.2 Gas phase

The continuity, momentum, and energy conservation equations define the Eulerian multiphase. Each stage is under control separately. A continuous model illustrates the gas phase. The mass conservation equation applies to every stage of the system's behavior. The model does not analyse the interaction between two phases; rather, it considers the gas phase at the beginning of a process [28]. Solving the particle's paths yields the source term. The gas phase is resolved by adding the source term to the equation, according to Ansys Fluent.

$$\frac{\partial}{\partial x_i}(\rho u i) = S_m \tag{6}$$

**Momentum:**

$$\rho u_i \frac{\partial u i}{\partial x i} = \frac{\partial}{\partial x j}\left[\mu\left(\frac{\partial u i}{\partial x j} + \frac{\partial u j}{\partial x i}\right) - \frac{2}{3}\mu\left(\frac{\partial u j}{\partial x j}\right)\delta i j\right] + \rho g i - \frac{\partial p}{\partial x i} + F i \tag{7}$$

**Energy**

$$\rho u i \frac{\partial e}{\partial x i} = -p \frac{\partial u i}{\partial x i} + \Phi v + \frac{\partial}{\partial x i}\left(k \frac{\partial T}{\partial x i}\right) + \frac{\partial}{\partial x i} \tag{8}$$

$$\rho u i \frac{\partial m i}{\partial x i} = -p \frac{\partial J_i}{\partial x_i} + S_m \tag{9}$$

$$J_i = -\rho D_{i,m} \frac{\partial m_i}{\partial x_i} \tag{10}$$

## 2.3 Standard k- ϵ model

The numerical representation of turbulence that is employed in real-world and industrial applications is known as turbulent flow. We used simple methods to estimate the expected changes in turbulence using the turbulence model.

The flow field of the combustor was solved using the k-$\varepsilon$ model. This model also fits the calculations of swirl and separated flow in the combustion chamber very well. It can also accurately predict complex swirls with low to medium intensity, like shear flow, separated flow, and swirling flow [28, 29]. We primarily compute this model using the Boussinesq assumption, which first links the Reynolds stress and average velocity gradient. We then determine the eddy viscosity coefficient by adding a formula and a new transport equation to the dissipation rate. The following are the turbulent transport equations.  Kinetic energy and dissipation- rate in the model [24]

$$\frac{\partial}{\partial t}(\rho k) + \frac{\partial}{\partial x_i}(\rho k u_i) = \frac{\partial}{\partial x_j}\left[\left(\mu + \frac{\mu_t}{\sigma_k}\right)\frac{\partial k}{\partial x_j}\right] + G_k + G_b - \rho\epsilon - Y_m + S_k \tag{11}$$

$$\frac{\partial}{\partial t}\rho\epsilon + \frac{\partial}{\partial x_i}(\rho \in u_i) = \frac{\partial}{\partial x_j}\left[\left(\mu + \frac{\mu_t}{\sigma_\epsilon}\right)\frac{\partial\epsilon}{\partial x_j}\right] + C_{1\epsilon}\frac{\epsilon}{k}(G_k + C_{3\epsilon}G_b) - C_{2\epsilon}\rho\frac{\epsilon^2}{k} + S_\epsilon \tag{12}$$

$$\mu_t = \rho C_m \frac{k^2}{\epsilon}, G_k = -\rho u'_i u'_j \frac{\partial u_j}{\partial x_i}, G_b = \beta g_i \frac{\mu_t}{Pr_t}\frac{\partial T}{\partial x_i} \tag{13}$$

The constants model is:

$C_{1\epsilon} = 1.44, C_{2\epsilon} = 1.92, C_m = 0.09, \sigma_k = 1, \sigma_\epsilon = 1.3, \sigma_{3\epsilon} = -0.33$

## 2.4 Combustion model

The present work employed the probability density function (pdf) to analyze various combustion properties. Two types of probability density functions can be made from the mixture fraction: a clipped Gaussian function and a beta function [30, 27]. These can be used to show how the turbulence changes the values of the conservation scalar. The current study often uses a beta function due to its affordability and versatility. Calculating the beta function using mathematics**:**

$$p(f) = \frac{f^{\psi-1}(1-f)^{B-1}}{\int_0^1 f^{\psi-1}(1-f)^{B-1}df} \tag{14}$$

$$f = \frac{z_i - z_{i,ox}}{z_{i,fuel} - z_{i,ox}} \tag{15}$$

The coefficients $\Psi$ and B are the explicit functions of the average mass mixture fraction (*f*) as well as the concentration fluctuation (g), as stated by:

$$\psi = f\left[\frac{f(1-f)}{g} - 1\right] \tag{16}$$

$$B = (1-f)\psi \tag{17}$$

Putting these amounts in proportion to a certain probability Once the *f ·* and *g* are determined from the finite difference solutions at each point on the grid, density helps users compute the species concentration mean values, output temperature, density, and enthalpy. the percentage of the mixture Functions of *p(f)* might have suitable parameters. The instantaneous mixture fraction *(f)* is represented by each of the following numbers: $y_i$ *(f)*, $H_i$ *(f)*, *T (f)*, and $\rho$ *(f)*. The Favre-averaging quantity *Q ˘* may be computed using these values.

$$\breve{Q} = \int_0^1 \breve{p}(f)Q(f)df \tag{18}$$

Additionally, after utilizing equations (16) and (17) for calculating *Ψ* and *p* from the indicated values of *(f)* and *(g)*, Beta PDF only depends on the Mixture Fraction. Suitable numbers, like N=100, of various amounts of *Yi (f)*, *T(f)*, and so on were tallied in tabular way and calculated from the state equations for the mixture fraction in the field (0-1).

## 2.5 NOx model

The most common constituents of NOx emissions are nitrous oxide (N2O), nitrogen dioxide (NO2), and nitric oxide (NO). [31]. There are several ways that NOx production might happen [26]. Thermal NOx, which results from the dissociation of nitrogen and oxygen molecules at very high temperatures, is one of the primary reasons for NOx generation. The Zeldovich mechanism is a collection of extremely temperature-dependent chemical processes that control the generation of thermal NOx. [32] [34].

$$O + N_2 \leftrightarrow N + NO$$
$$N + O_2 \leftrightarrow O + NO$$
$$N + OH \leftrightarrow H + NO$$
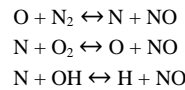
The following formula is used to determine the thermal-NO creation rate:

$$\left(\frac{d[NO]}{dt}\right) = 2k_{f.R14}[O][N_2]\frac{\left(1 - \frac{k_{r.R14}k_{r.R15}[NO]^2}{k_{f1.R14}[N_2]k_{f.R15}[O_2]}\right)}{\left(1 + \frac{k_{r.R14}[NO]}{k_{f.R15}[O_2]k_{f.R16}[OH]}\right)} \tag{19}$$

Experimental investigations have determined the rate coefficients for the chemical equations included in the NOx model, as well as the rate constants for chemical reactions as follows:

*$k_{f,1}$= 1.8 \*108 e -38370/T*     *$k_{r,1}$= 3.8 \*107 e -425/T*
*$k_{f,2}$= 1.8 \*104 T e-4680/T*     *$k_{r,2}$= 3.81 \*103T e-20820/T*
*$k_{f,3}$= 7.1 \*107 e-450/ T*     *$k_{r,3}$= 1.7 \*108 e-24560/T*

$k_f$ and $k_r$ represent forward reactions rete constants and their units *(m3/gmol-s)*, so the NOx formation rate must be calculated using the concentrations of (O), (OH), and (H)The mass transport equations of the nitrogen-containing species have source terms that return the total rates to the fluent solver via the Pollute structure.[32][33]

$$\frac{\partial}{\partial t}(\rho\gamma_{HCN}) + \nabla \cdot (\rho\vec{v}\gamma_{HCN}) = \nabla \cdot (\rho D\nabla\gamma_{HCN}) + S_{HCN} \tag{20}$$

$$\frac{\partial}{\partial t}(\rho\gamma_{NO}) + \nabla \cdot (\rho\vec{v}\gamma_{NO}) = \nabla \cdot (\rho D\nabla\gamma_{NO}) + S_{NO} \tag{21}$$

$$\frac{\partial}{\partial t}(\rho \gamma_{NH3}) + \nabla \cdot (\rho \vec{v} \gamma_{NH3}) = \nabla \cdot (\rho D \nabla \gamma_{NH3}) \tag{22}$$

$$[O] = 3 \cdot 97 * 10^5 \ T^{-1/2} [O_2]^{1/2} \ e^{-31090/T} \tag{23}$$

$$[OH] = 2 \cdot 129 * 10^2 \ T^{-0.57} e^{-4595/T} [O_2]^{1/2} [H_2O]^{1/2} \tag{24}$$

## 3. Numerical method

Ansys Fluent 15.0 solves the governing equations. The pressure-based stable solver has also solved two-dimensional geometry in the Cartesian coordinate system. The SIMPLE algorithm has made an association between pressure and velocity. Equations involving momentum and mixture fractions use the power law to separate the variables. This method reduces the energy equation to discrete form, thereby second-ordering the results. After the solution's final grid independence test, we have performed discrete-phase and continuous-gas-phase simulations. We perform 300 continuous-phase iterations for every discrete-phase iteration. Additionally, 150 iterations after NOx prediction.

This research specifically examines spray combustion in a non-premixed turbulent combustion process. In order to validate our findings, we conducted a comparison between the test cases and the experimental data acquired by Moa et al. (35). The n-pentane-air spray, Fig.1 creates a flame that consists of two distinct zones. We refer to the first region at the bottom as the flame cone, and the subsequent region above, characterized by a longer area, as the development zone.

This bears resemblance to the findings reported by Mao et al. (35). The cylindrical structure of the combustion chamber measures 10 meters in length and 1 meter in diameter. An injector measuring 0.2 m in diameter introduces the n-pentane fuel into the system, while an injector with a diameter of 0.49 micron introduces the air**.** Figure 1 displays the geometric properties, while Table 1 provides the boundary conditions. The boundary conditions pertaining to the measurements conducted by Mao et al. (35) serve as the foundation for a comprehensive simulation of a 2-D test scenario. We can validate the findings from the computational fluid dynamics (CFD) simulation by comparing them with the measurements and experimental data. The validation computation takes into account the spray droplet's input parameters. The parameters and gas phase measurements are comparable. Table 2 provides the relevant boundary and operating conditions for the liquid and gas characteristics. According to the Cartesian coordinate system, the arrangement exhibits symmetry. To define the geometry and generate the 2D grid, we use the "GAMBIT" program. The study considered refining the zones around the burner output in order to capture various phenomena that may occur within these zones, namely the variations in characteristics, as seen in Fig.2a, b, and c **.** The study performs computations on multiple grids. We evaluate the grid's convergence, its impact on the outcomes, and select the grid to use in this study. We conduct multiple experiments by manipulating the grid's dimensions, quantity, and arrangement within the computational domain. We ran a set of computations for each research instance, utilizing three revised structured grids across the entire domain. The chosen instance is case C, which consists of 83200 cells, 167304 nodes, and 84105 faces. Table 3 presents the grid's parameters. Figure 2d presents a comparative analysis of the experimental outcomes obtained at various grid modifications. The diagram illustrates the gas flame temperature curve under various scenarios. The

grid density has a significant impact. Consequently, we may infer that the answer relies on the grid.

**Table 1.** Experimental conditions taken from Mao et al. (35)

| Fuel | n -Pentane | Unite |
|---|---|---|
| Injection pressure | 02.67 | MPa |
| Injection duration | steady | ms |
| Injection quantity | 04.00 | ml |
| Souter mean diameter | 28.00 | μm |
| Ambient gas | Air | |
| Maximum-drop diameter | 79.00 | μm |
| Injector diameter | 00.20 | μm |
| Spray injection velocity | 69.00 | m/s |
| Ambient pressure | 3.2 , 6.3 , 9.4 | MPa |

**Table 2.** Operating condition

| Parameters | Value | Units |
|---|---|---|
| Injector inlet and ambient Temp. | 296 | K |
| Injector diameter | 1.194 | mm |
| Initial velocity of air | 11.6 | m/s |
| Initial velocity of fuel | 69 | m/s |
| Reynolds number | 3600 | ----- |
| Air temp. | 1255 | K |
| Air mass flow rate | 0.08-0.225 | Kg/s |

**Table 3.** The grid details

| Details | Coarse mesh | Medium mesh | Refine mesh |
|---|---|---|---|
| **CELL** | 5200 | 20800 | 83200 |
| **Faces** | 10626 | 42052 | 167304 |
| **Nodes** | 5427 | 21253 | 84105 |
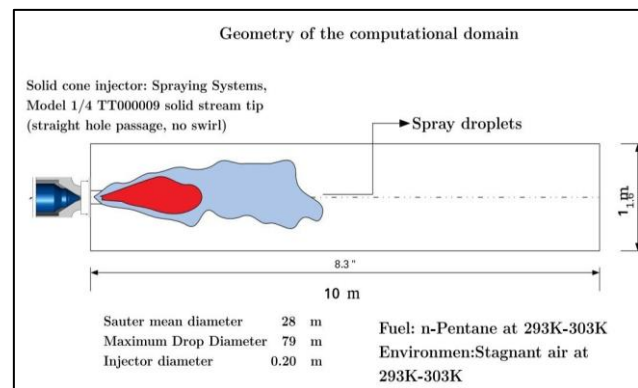


**Figure 1.** Schematic of the combustor.

**a-coarse mesh**



**b-Medium mesh**



**c-Refine mesh**



**(d)**

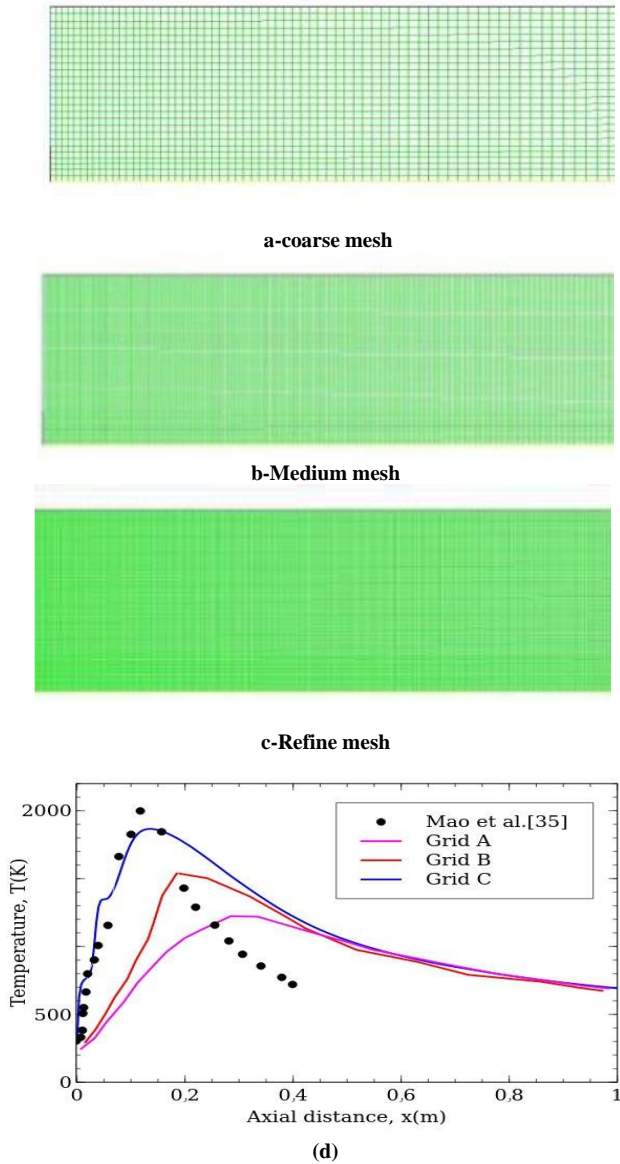**Figure 2.** Coarse grid (a), Medium grid (b), Fine grid (c), Comparison between the gas temperature with experimental data of Mao et al. [35] at different grid resolutions(d) .

## 4. Results and discussions

The significant thermal NOx model was used in this work to determine the formation of NOx in cases before and after NOx prediction, where after represents two OH models (none and partial). The spray droplet injection settings are taken from Mao et al. [35]. Temperature contours along the combustor axis in vertical planes are shown in Fig. 3a-b, together with the axial distance in m. The area of high temperature that appears in the combustor can represent the flame zone. However, the data indicates that, in the case after NOx (Case a), the combustion chamber flame is comparatively long. The tangential entry of the primary flow surrounds the combustor's axis. Under the effect of flow, the injected fuel evaporates,

reacts with air, and moves axially forward to burn around the central axis. As a result, the area where the flame grows downwind of the central axis has the highest temperature. In this instance, the region of high temperature that develops in the combustor can represent the highest temperature in the flame zone. The combustion chamber's flame, which is 0.15 meters from the combustor's inlet plane and estimated to be 1900 K, is comparatively long for the case with NOx (Case a), according to the statistics. The contours of maximum temperature, which depict the flame zone, stay on the axis but move in close proximity to the entry Fig. 3b. A comparison of the static temperatures with NOx and without NOx prediction versus Mao et al. [35] is shown in Fig. 4.
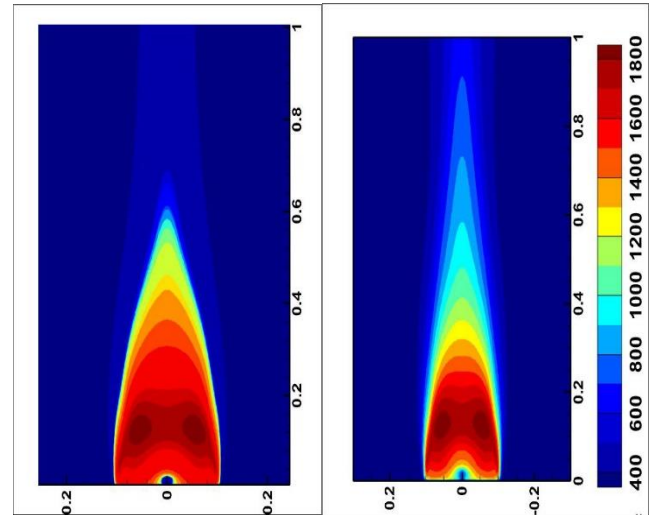


**Figure 3.** Shows the static temperature contour plots (before(b) and after(a) NOx prediction) along the axis of symmetry.
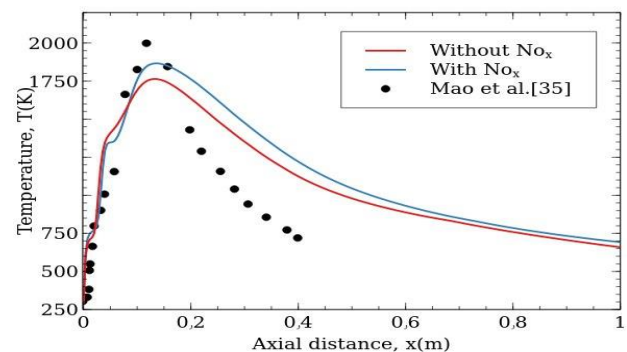


**Figure 4.** Comparison of the flame temperature without NOx with NOx and the experimental data of Mao et al. [35] along the axis of symmetry.

The hydrodynamic and chemical processes between the two phases are causing these profiles to attain their greatest values close to the nozzle area. Compared to Mao et al., it is clear that the trend at the beginning has a fairly similar arrangement with and without NOx [30]. but then it starts to diverge. In the case of NOx findings, the temperature discrepancy between the numerical simulation and Mao et al. [35] is 0.05%, whereas in the case of results without NOx, it is 0.175%. Figure 4 also explains the midline temperature change in a turbulent n-pentane vapor-air diffusion flame

based on measurements, current predictions, and the injection conditions of spray droplets at the nozzle region, The temperature reports a high level. It then increases fast until it reaches its highest value, which is roughly 1900 K after NOx prediction and 1650 K before NOx prediction at 0.15 m from the inlet. After that, it decreases sharply to 400 K, where it is at this value. The Fig. 5 illustrates the evaluation of flame temperature along the axis of symmetry and in two lines which enables the detection of differences between the before and after NOx formation cases. There is a noticeable rapid rise in temperature instances at x = 0.1 m in the axial temperature profiles. The three radial lines, the center line, and the line at the domain's edge are utilized to calculate the temperature differences. The radial lines are positioned at x = 0.1 m, x = 0.3 m, and x = 0.5 m on the x-axis to provide a mapping of the research variables at various flame locations. When x = 0.15 m, the largest difference appears**.**
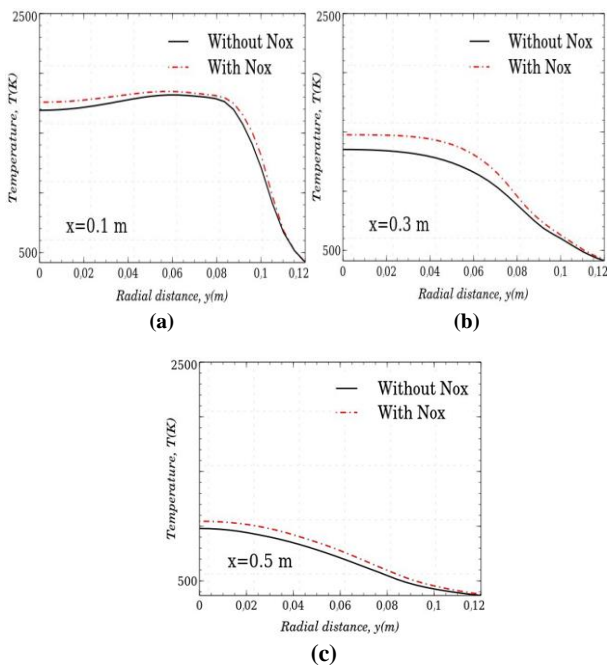


**Figure 5.** Radial profiles of flame temperature without Nox with Nox at (a) x = 0.1 m, (b) x = 0.3 m, (c) x = 0.5m

The x-velocity component along the centreline is shown in Fig. 6 Due to the droplet at the nozzle orifice evaporating, the x-velocity component of the gas phase first reduces and then rises as the gas density is reduced. Both before and after the NOx prediction, at (0 < x < 10) cm, the axial distance and the intersection point at a certain location diverged. They reached the lowest possible velocity values at x = 10 cm when comparing the two cases. The spray droplets burn to a single phase at x > 10 cm in each case. The numerical simulation for the scenario with NOx and the case without NOx shows a discrepancy of 0.071% in axial velocities. The x-velocity component tends to rise and roughly converge as seen in Fig. 7 NOx formation has little effect on flame velocity. Regarding spray flame velocity, the data show no discernible variation. The results are influenced by the gas velocity distance from the injector outlet. The location lines x = 0.1 m show the largest difference compared with other lines. At x= 0.3 the gas velocity for both cases before and after NOx formation are converge

then become identical at y=0.08 and x=0.05 m as a result, the OH model may have a little impact on gas velocity. The gas phase's turbulence dissipation rate profiles along the centreline before and after the NOx prediction are shown in Fig. 8. The NOx prediction has little effect on the turbulence dissipation rate, as seen by the comparison of the high dissipation rates obtained before and after the prediction. In order to determine variations between the cases before and after NOx generation, the numerical simulation for the scenario with NOx and the case without NOx shows a discrepancy of 0.05% in axial turbulence dissipation rates. Figure 9 shows the evaluation of turbulence dissipation rate along the radial axis and in two lines. The turbulence dissipation rate in the profiles increases somewhat until it reaches y = 0.04 m, at which point it decreases until it equals zero. To compute the turbulence dissipation rate differences, three radial lines, the centred line, and the line at the boundary of the domain are used. The radial lines were positioned at x = 0.1 m, x = 0.3 m, and x = 0.5 m on the x-axis to create a mapping of the research variables at various positions The turbulent kinetic energy distributions near the centreline of the gas phase are shown in Fig. 10 before and after the NOx prediction.
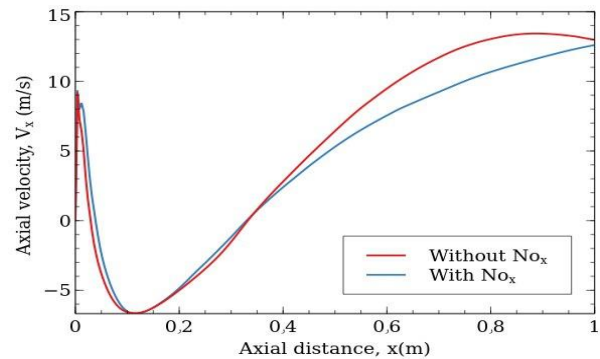


**Figure 6.** Variation of axial velocity without NOx with NOx along the axis of symmetry.

As the next state is far from the nozzle, a lot of turbulent kinetic energy builds up. This energy is then pushed downstream and spread out across the nozzle region in a way that interacts with the liquid and gas phases. There is a difference of 0.21 percent in the axial turbulence kinetic energy between the NOx scenario and the no-NOx case in the numerical simulation**.** Figure 11 shows that similar results are obtained in the case before NOx, but with less intensity. To tell the difference between what happened before and after NOx production, the turbulent kinetic energy for the gas phase is found in two lines and along the radial axis. To determine the differences in turbulent kinetic energy, three radial lines, a central line, and a line at the domain's boundary are used. To get the study variables at different locations, the radial lines are positioned on the x-axis in the following manner: at x = 0.1 m, x = 0.3 m, and x = 0.5 m. Around the nozzle area at x = 0.1 m, the turbulent kinetic energy dissipated through an interaction between the liquid and gas phases. Because of its distance from the nozzle, it is rejected downstream**.** Figure 12 shows the NOx mass fraction for the partial and non-OH models. The effect of OH models has been calculated at different positions within the combustion chamber, and the parameters for both models are similar.
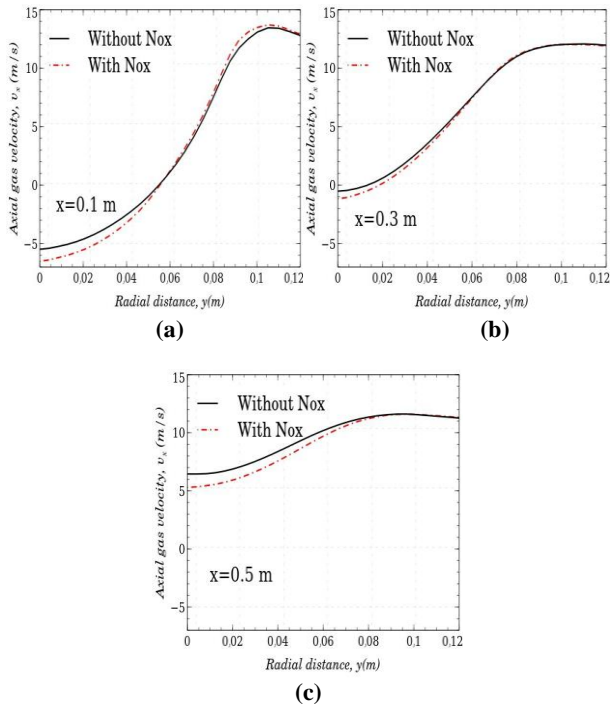
**(a)**

**(b)**



**(c)**

**Figure 7.** Radial profiles of spray axial velocity at (a) x = 0.1 m,
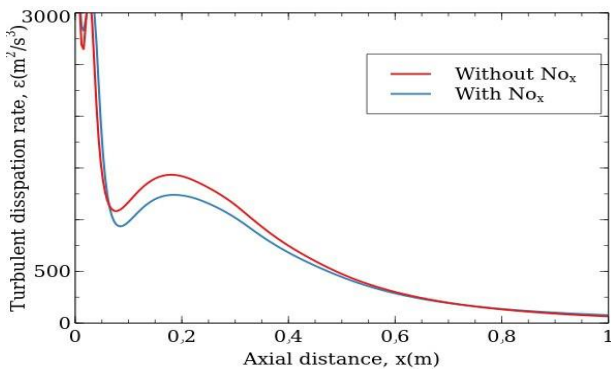(b) x = 0.3 m, (c)x = 0.5m



**Figure 8.** Turbulent dissipation rate without NOx and with NOx
along the axis of symmetry.

However, changing the model has not much of an effect on the NOx mass fraction with respect to axial distance; the partial model is higher than the none model. At 0.15 meters from the inlet, the partial NOx mass fraction reached its maximum at roughly (5.5 E-05) and (5 E-05) for the none model. The difference in NOx mass fraction between the partial model and the non-OH model is 0.09%. Figure 13a-b depicts NOx mass fraction contours over the combustor axis in vertical planes, for the cases none(a) and partial(b) OH model. The figure shows that the flame in the combustion chamber is relatively long for the case partial (Case b). Figure 14 displays the assessment of the NOx mass fraction along the axis of symmetry and in two lines allowing differences between the two models of OH (partial and none) to be identified. The NOx mass fraction in the profiles grows gradually and it is noticeable that the OH model has minimal influence. Each models of (OH) is almost the same at x = 0.3 m and the models are likewise equal at

x = 0.5 m. Three radial lines are used: the centred line, the line at the domain border, and the line at the NOx mass fraction discrepancies.
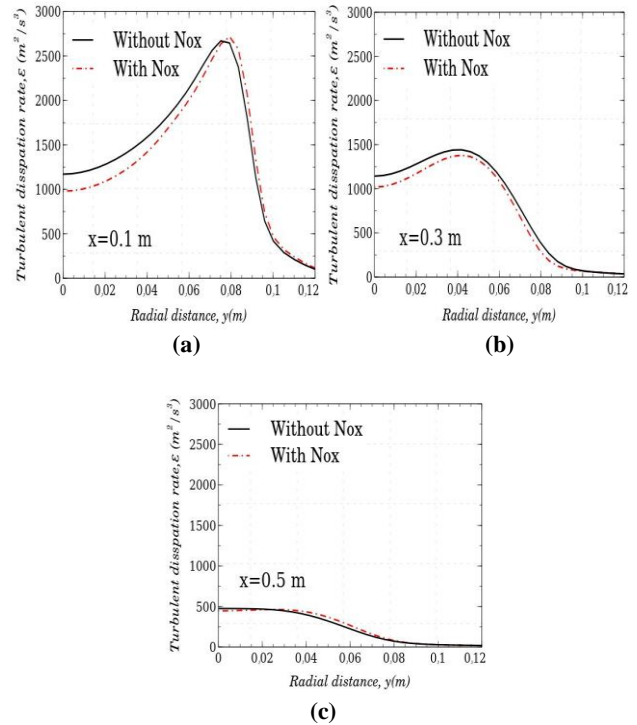


**(a)**

**(b)**



**(c)**

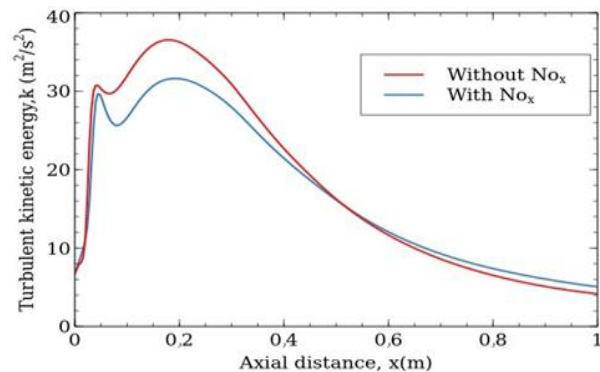**Figure 9.** Radial profiles of turbulent dissipation rate at (a) x = 0.1 m, (b) x = 0.3 m, (c)x = 0.5m.



**Figure 10.** Turbulent kinetic energy for case with NOx and without NOx along the axis of symmetry.

A comparison of the NOx rate in the partial and non-OH models is shown in Fig. 15. The parameters for both models are identical and the influence of the OH models has been computed at various positions within the combustion chamber. Nevertheless, the partial model is greater than the none model, and changing the model has little effect on the NOx rate with regard to axial distance. The partial NOx rate peaked at about 1.05 E-05 and 9.5 E-06 for the none model at 0.15 meters from the inlet and the difference in NOx rate between the partial model and the non-OH model is 0.09%.
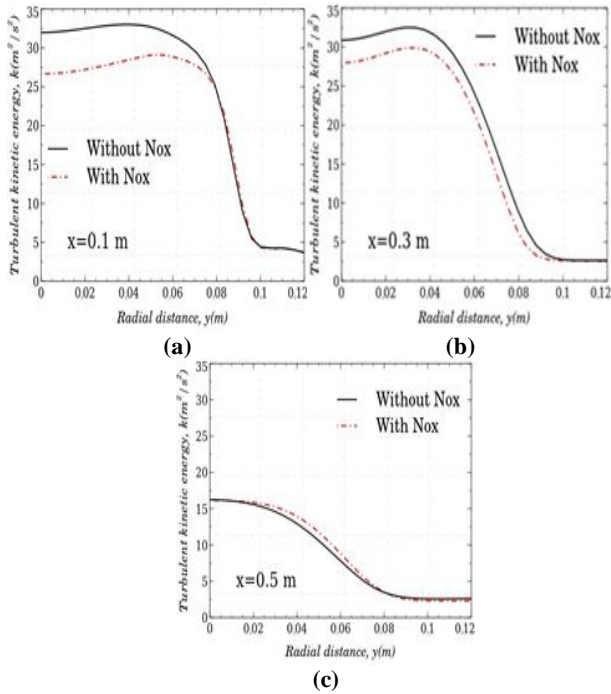
**Figure 11.** Radial profiles the turbulent kinetic energy at (a) x = 0.1 m, (b) x = 0.3 m, (c)x = 0.5m

Figure 16 shows the evaluation of NOx rate in two lines and along the radial axis, making it possible to distinguish between the two models of OH (partial and none). The profiles show a progressive increase in the NOx rate with little change according to the OH model at x = 0.1 m. Each of the models is practically identical at x = 0.3 m and they are also identical at x = 0.5 m. NOx rate contours over the combustor axis in vertical planes for the models of the none (a) and partial (b) OH models are shown in Fig. 17a-b. The figure (b)demonstrates how the combusting chamber's flames in this model are larger than in the (a) model.

In the future, we will study the prompt NOx prediction model, and we will compare thermal and prompt NOx prediction to detect the best model that has the fewest emissions.
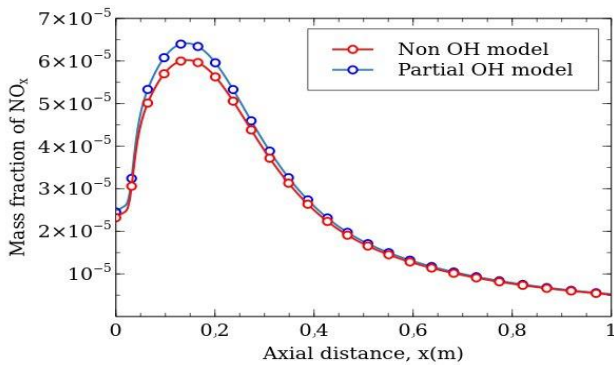


**Figure 12.** axial profile of NOx mass fraction for various OH model along the axis of symmetry.
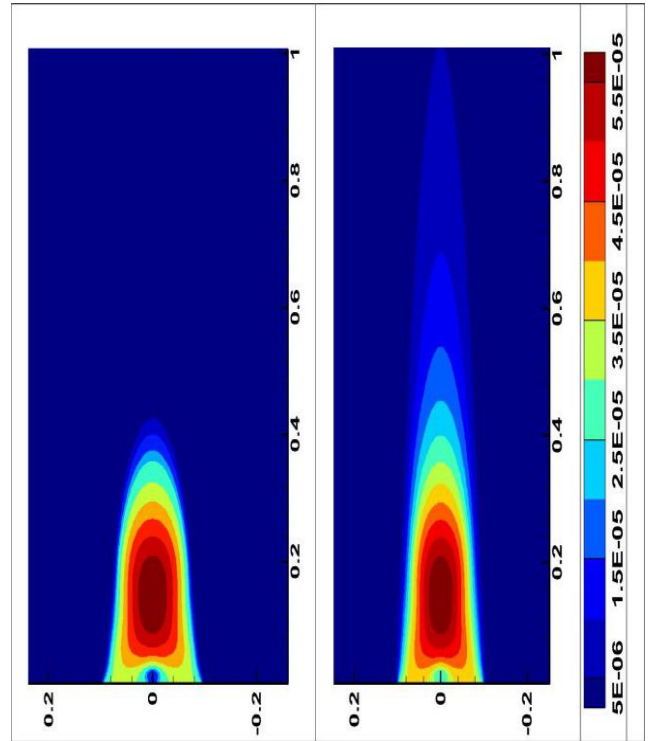


**Figure 13.** Contour plots of NOx mass fraction in ((a)none and (b) partial) OH model.
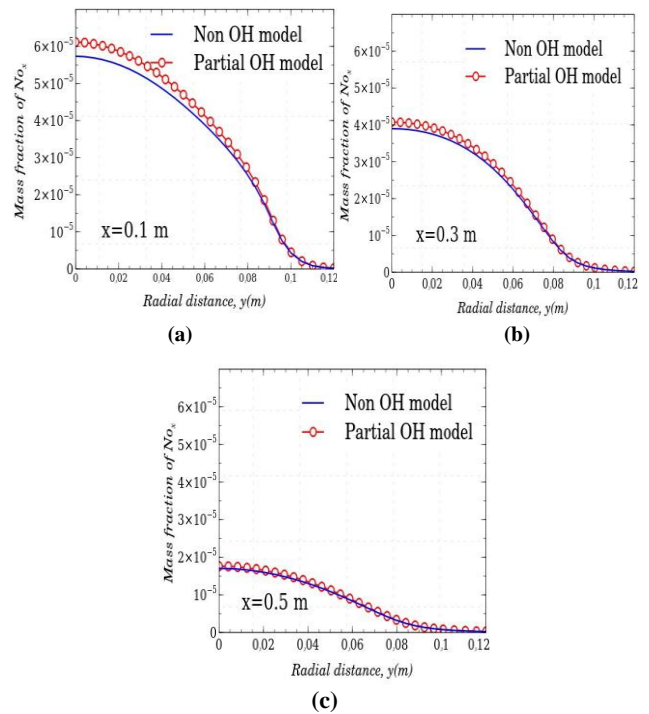


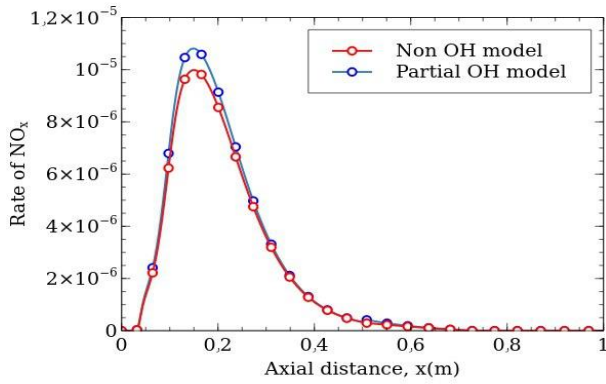**Figure 14.** Radial profiles of NOx mass fraction at (a) x = 0.1 m, (b) x = 0.3 m, (c)x = 0.5m

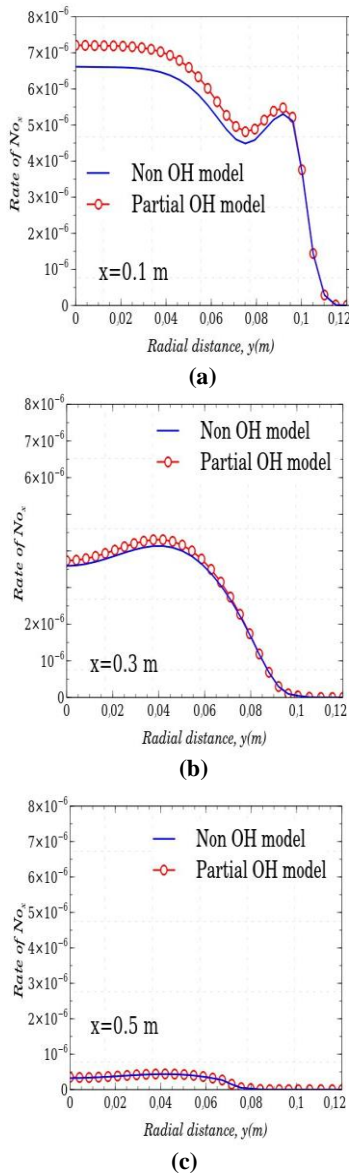**Figure 15.** The NOx rate for (parial and none )OH model along the axis of symmetry.



**(a)**



**(b)**



**(c)**

**Figure 16.** Radial profiles of NOx rate at (a) x = 0.1 m, (b) x = 0.3
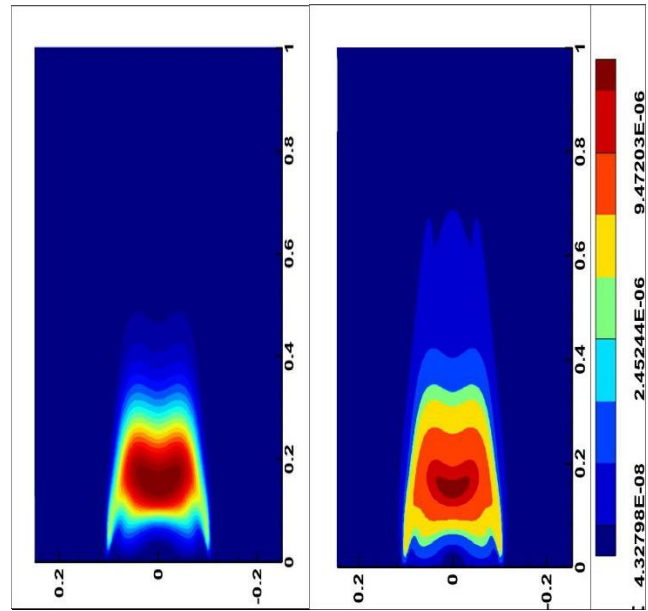


**Figure 17.** Contour plots of NOx rate in ((a)none and (b) partial) OH model.

## 5. Conclusion

Two OH models were used to simulate the two-dimensional steady-state spray combustion: partial and none. The research done is based on a comparative comparison of two states: the state of the partial OH model after the NOx forecast and the state of the none model, assuming that the O model was in equilibrium. The numerical models were verified using the available experimental data from Mao et al. (35). The axisymmetric models describe liquid fuel spread out in a Eulerian framework using the Lagrangian method and the Navier-Stokes equations. The flow was assumed to be steady and incompressible. The objective of this research was to investigate the impact of different OH models on steady-state spray combustion. Additionally, this study considers variations in gas phase velocity components, NOx mass fraction, NOx rate, turbulence kinetic energy, and turbulence dissipation rate. As a result, we performed a quantitative analysis of NOx production from $C_5H_{12}$ using the thermal NOx mechanism. The steady-state revealed similarities between the partial and instantaneous OH models. The study's findings lead to the following conclusions:

- The non-OH model has a lower value then the partial model. The results suggest that the OH model had little impact on the production of NOx in this specific situation.
- The temperature varied per the predicted NOx levels but remained consistent with the OH model's variability. The temperature peaked at 0.15 m from the inlet, with a value of around 1900 K after NOx prediction and 1650 K before NOx prediction.
- The NOx prediction has little impact on the velocity, turbulence dissipation rate, and turbulent kinetic energy obtained before and after it.
- Between the NOx and non-NOx cases, there is a difference of 0.05% in axial turbulence dissipation rates, 0.21% in turbulent kinetic energy, and 0.07% in axial velocity.

- Regarding the disparities between the conditions before and after the formation of nitrogen oxides (NOx), it is evident that the partial model has a higher value compared to the non-model. There is a 0.09% discrepancy in the NOx mass fraction between the partial model and the non-OH model. We conducted a comprehensive analysis and found that none of the OH models can be considered as the most optimal.

## Authors' contribution

All authors contributed equally to the preparation of this article.

## Declaration of competing interest

The authors declare no conflicts of interest.

## Funding source

This study didn't receive any specific funds.

## Data availability

The data that support the findings of this study are available from the corresponding author upon reasonable request.

## REFERENCES

[1] J. Warnatz, U. Maas and R.W. Dibble, COMBUSTION: Physical and Chemical Fundamentals, Modeling and Simulation, Experiment, Pollutant formation, 4th ed., Springer, 2006 https://doi.org/10.1007/978-3-540-45363-5_19

[2] R.W. Schefer, D.M. Wicksall and S.K.Aggarwal, "Combustion of Hydrogen-Enriched Methane in A Lean Premixed Swirl Stabilized Burner", Proceedings of the Combustion, Vol. 29, 2002, pp. 843- 851.z

[3] Y.B. Zeldovich and P.Y. Sadovnikov, Oxidation of Nitrogen in Combustion, Science Academy of USSR,1947.

[4] L. Lazic, M.A. Varga and J. Kizek "An Experimental Study of the Influence of FGR on NOx Formation", Material in Technology, Vol. 38, No. 5, January 2004, pp. 269–274.

[5] A. Cavaliere, M.D. Joannon, "Mild Combustion", Progress in Energy and Combustion Science, Vol. 30, 2004, pp. 329-366. https://doi.org/10.1016/j.pecs.2004.02.003

[6] J.A. Wünning, J.G. Wünning, "Flameless Oxidation to Reduce Thermal NO-Formation", Progress in Energy Combustion Science, Vol. 23, 1997, pp. 81-94.

[7] ]F. Hu, P. Li, J. Guo, Z. Liu, L. Wang and et al., "Global Reaction Mechanisms for MILD Oxy-Combustion of Methane", Energy, Vol. 147, 2018, pp. 839–857 .https://doi.org/10.1016/j.energy.2018.01.089

[8] Y. Tu, K. Su, H. Liu, Z. Wang, Y. Xie, C. Zheng and et al., "MILD Combustion of Natural Gas using Low Preheating Temperature Air in an Industrial Furnace", Fuel Processing Technology, Vol. 156, 2017, pp. https://doi.org/10.1016/j.fuproc.2016.10.024

[9] H. Bordbar, A. Maximov, T. Hyppnen, Improved banded method forspectral thermal radiation in participating media with spectrally dependent wall emit- tance, Applied Energy 235 (2019) 10901105, https://doi.org/10.1016/j.apenergy.2018.11.033

[10] M.R. Shakeel, Y.S. Sanusi and E.M. Mokheimer, "Numerical Modeling of Oxy-Fuel Combustion in a Model Gas Turbine Combustor: Effect of Combustion Chemistry and Radiation Model", Energy Procedia, Vol. 142,2017, pp. 1647-1652. https://doi.org/10.1016/j.egypro.2017.12.544

[11] M.H. Bordbar, G. Wecel and T. Hyppanen, "A Line by Line Based Weighted Sum of Gray Gases Model for Inhomogeneous CO2-H2O Mixture in Oxy-fired Combustion", Combust Flame, Vol. 161, 2014, pp. 2435– https://doi.org/10.1016/j.combustflame.2014.03.013

[12] C.V. Silva, F.H. R. Franca and H.A. Vielmo, "Analysis of the Turbulent, Non-Premixed Combustion of Natural Gas in a Cylindrical Chamber with and without Thermal Radiation", Combustion Science and Technology, Vol. 179, No. 8, 2007, pp. 1605–1630 https://doi.org/10.1080/00102200701244710

[13] 1-S. Hayashi, and H. Yamada, 2000, "NOx emissions in combustion of lean premixed mixtures injected into hot burned gas," Proceedings of the Combustion Institute, 28:2443–2449. https://doi.org/10.1016/S0082-0784(00)80658-X

[14] Y. Tu, H. Liu, S. Chen and et al., "Effect of Furnace Chamber Shape on MILD Combustion of Natural Gas", Applied Thermal Engineering, 2014, pp.1-12 https://doi.org/10.1016/j.applthermaleng.2014.11.007

[15] 2- S. Hayashi, H. Yamada, and M. Makida, 2005, "Extending low-NOx operating range of a lean premixed-prevaporized gas turbine combustor by reaction of secondary mixtures injected into primary stage burned gas," Proceeding of the Combustion Institute, 30:2903-2911. https://doi.org/10.1016/j.proci.2004.08.112

[16] J. Mi, F. Wang, P. Li and B.B. Dally, "Modified Vitiation in a Moderate or Intense Low Oxygen Dilution (MILD) Combustion Furnace", Energy & Fuels, 2012, pp. 265-277. https://doi.org/10.1016/j.proci.2004.08.112

[17] P. Li, J. Mi, B.B. Dally, R.A. Craig and F. Wang, "Premixed Moderate or Intense Low Oxygen Dilution (MILD) Combustion from a Single Jet Burner in a Laboratory Scale Furnace", Energy & Fuels, 2011, pp. 2782-2793. https://doi.org/10.1021/ef200208d

[18] J. Mi, P. Lit, B.B. Dally and R.A. Craig, "Importance of Initial Momentum Rate and Air-Fuel Premixing on Moderate or Intense Low Oxygen Dilution (MILD) Combustion in a Recuperative Furnace", Energy & Fuels, 2009, pp. 5349–5356 https://doi.org/10.1021/ef900866v

[19] L. Bo, W. Yuanhua and X. Hong, "Numerical Study of Air Nozzles on Mild Combustion for Application to Forward Flow Furnace", China Petroleum Processing and Petrochemical Technology, 2016, pp. 108-122 .http://www.chinarefining.com/EN/

[20] D. Perrone, T. Castiglione, P. Morrone, S. Barbarelio and M. Amelio, "NOx Emissions for Oxy-Mild Combustion of Pulverized Coal High Temperature Pre-Heated Oxygen", Energy Procedia, Vol. 148, 2018, pp. 567-574 https://doi.org/10.1016/j.egypro.2018.08.143

[21] B. Masum, H. Masjuki, M. Kalam, I. R. Fattah, S. Palash and M. Abedin" Effect of ethanol–gasoline blend on NOx emission in SI engine" Renewable and Sustainable Energy Reviews 2013 Vol. 24 Pages 209-222 https://doi.org/10.1016/j.rser.2013.03.046

[22] D. Cerinski, M. Vujanović, Z. Petranović, J. Baleta, N. Samec and M. Hriberšek " Numerical analysis of fuel injection configuration on nitrogen oxides formation in a jet engine combustion chamber" Energy conversion and management 2020 Vol. 220 Pages 112862 https://doi.org/10.1016/j.enconman.2020.112862

[23] S. Sharma, R. Kumar, A. Chowdhury, Y. Yoon and S. Kumar " On the effect of spray parameters on CO and NOx emissions in a liquid fuel fired flameless combustor" Fuel 2017 Vol. 199 Pages 229-238 https://doi.org/10.1016/j.fuel.2017.02.102

[24] M. D. Bohon and W. L. Roberts " NOx emissions from high swirl turbulent spray flames with highly oxygenated fuels" Proceedings of the Combustion Institute 2013 Vol. 34 Issue 1 Pages 1705-1712 https://doi.org/10.1016/j.proci.2012.07.064

[25] M. Xu, Y. Tu, G. Zeng, Q. Wang, A. Zhou and W. Yang " Numerical study of further "NOx emission reduction for coal MILD combustion by combining fuel‐rich/lean technology" International Journal of Energy Research 2019 Vol. 43 Issue 14 Pages 8492-8508 https://doi.org/10.1002/er.4849

[26] S. Pope, Combustion Modelling using Probability Density Function Methods, Numerical Approaches to Combustion Modelling, Prog. Astronaut. Aeronaut, AIAA, 1991

[27] Majhool, A.A.A.K., *A comparative study of radiation models in spray combustion.* Al-Qadisiyah Journal for Engineering Sciences, 2023. **16**(1).

[28] Majhool, A.A. and D.Y. Haran, Application of LES/PDF and RANS/PDF approaches for simulation of spray combustion. Al-Qadisiyah Journal for Engineering Sciences, 2021. 14(2).

[29] S. Morsi , A. Alexander , An investigation of particle trajectories in two-

phase 208 systems, Journal of Fluid mechanics, vol. 55, no. 2, pp. 193- 208, 1972 https://doi.org/10.1017/S0022112072001806

[30] Bojko, B.T. and P.E. DesJardin, On the development and application of a droplet flamelet-generated manifold for use in two-phase turbulent combustion simulations. Combustion and Flame, 2017. 183: p. 50-65. https://doi.org/10.1016/j.combustflame.2017.04.029

[31] CFD Predictions of Low NOx Radial Swirlers with Central Fuel Injection, PT King, HS Alkabie, GE Andrews, MM Pourkashanian and AC McIntosh, ASME Paper GT2009-60106,2009 https://doi.org/10.1115/GT2009-60106

[32] Mohsen, M.J. and M.F. Al-Dawody, The combustion characteristics of compression ignition engine fuelled partially by LPG-Diesel blends (Simulation study). Al-Qadisiyah Journal for Engineering Sciences, 2022. 15(3).

[33] Xu, M., et al., Numerical study of further NOx emission reduction for coal MILD combustion by combining fuel‑rich/lean technology International Journal of Energy Research, 2019. 43(14): p. 8492-850 https://doi.org/10.1002/er.4849

[34] J. Blauvens, B. Smets, and J. Peters. In 16th Symp. (Int'l.) on Combustion The Combustion Institute. 1977.

[35] Y.B. Zel'dovich (1946). "The Oxidation of Nitrogen in Combustion Explosions". Acta Physicochimica U.S.S.R. 21: 577–628 https://doi.org/10.1252/kakoronbunshu.26.127

[36] C.-P.Mao, G. Szekely Jr, G. Faeth, Evaluation of a locally Homogeneous model of spray combustion, Journal of Energy, vol. 4, no. 2, pp.78-87, 1980 model of spray combustion, Journal of Energy, vol. 4,no. 2, pp.78-87, 1980 K. https://doi.org/10.2514/3.48017